Asia-Pacific Journal of Science and Technology: Volume: 29. Issue: 06. Article ID.: APST-29-06-05. Research Article

APST

Asia-Pacific Journal of Science and Technology

https://www.tci-thaijo.org/index.php/APST/index

Published by the Research Department,
Khon Kaen University, Thailand

The influence of wave height and period on airflow velocity and differential pressure in L-shaped oscillating water column (L-OWC) chamber for wave energy converter (WEC)

Adnan S. D. Marta[1,2], Deendarlianto[1,*], Widjo Kongko[2], Indarto[1], Fauzun[1] and Ahmad T. Rohman[3]

[1]Department of Mechanical and Industrial Engineering, Faculty of Engineering, Universitas Gadjah Mada, Yogyakarta, Indonesia
[2]Research Center for Hydrodynamics Technology, National Research and Innovation Agency, BRIN, Surabaya, Indonesia
[3]Research Center for Energy Conversion and Conservation, National Research and Innovation Agency, BRIN, Surabaya, Indonesia
[*]Corresponding author: deendarlianto@ugm.ac.id

Received 13 September 2023
Revised 16 October 2023
Accepted 12 March 2024

Abstract

The Oscillating Water Column (OWC) technology is widely recognized as a highly efficient solution for harnessing wave energy and has shown significant progress. In this context, the OWC device with an L-shaped chamber, recently introduced and developed by Wave Swell Energy Australia, has garnered significant interest from researchers in the field of marine energy. This device stands apart from conventional OWCs or other models due to its utilization of an L-shaped channel for capturing wave energy. This research aims to understand the influence of wave height and wave period on airflow velocity and pressure differentials within the L-shaped OWC chamber and to obtain the efficiency value of the L-shaped OWC (L-OWC) chamber with variations in input wave generation characterized by relatively short-wave periods. The research was conducted using numerical simulations with Flow 3D software version 11, validated through 2D physical model testing at the Coastal Dynamics Laboratory - National Research and Innovation Agency (1:8 scale). The numerical study observed that wave height and wave period significantly affect the airflow velocity and differential air pressure within the L-OWC chamber. The L-OWC effectively harnesses energy optimally with wave periods longer than 2.47 seconds. The L-OWC chamber design demonstrates optimization at a T_{in} period of 2.47 seconds, with an average efficiency of 84.2% across various wave height scenarios. The peak power efficiency of the L-OWC device is 98.2%, achieved with a H_{in} variation of 0.1875 m and T_{in} of 2.47s.

Keywords: Oscillating water column, L-OWC, Airflow velocity, Differential pressure, CFD, power efficiency.

1. Introduction

Wave energy offers numerous benefits: it boasts one of the highest energy density rates and has minimal environmental impact. Additionally, waves are an enduring and predictable energy source that can traverse vast distances without energy loss [1,2]. Among the various technologies under investigation, the oscillating water column (OWC) stands out as a wave energy extraction system that utilizes the movement of incoming ocean waves to drive an oscillating column housed within a pneumatic chamber connected to the sea [3]. The configuration of the OWC chamber indeed impacts the efficiency of the OWC type Wave Energy Converter (WEC) system. Studies have shown that the configuration of the OWC chamber affects the volumetric volume of compressed and pumped air, affecting the amount of power produced by the wind turbine [4]. Studies have indicated that the optimal geometry for the OWC chamber typically involves a specific ratio of room height to room width. This ideal ratio facilitates efficient air compression, leading to optimal power generation. Additionally, research has revealed that increasing the ratio of chamber height to chamber width further enhances compression efficiency, thereby improving the overall performance of the system [5].

The geometry of the OWC chamber significantly affects the effectiveness of the OWC device [6,7]. The energy the LIMPET OWC device generates is greater when exposed to larger incident wave heights. Increased incident wave heights lead to the generation of more vortices at the lower edge of the device chamber's front wall [8]. In a numerical study conducted by Samak et al. (2021), an examination was carried out to assess how replacing a basic front wall with an L-shaped front wall influences the efficiency of the OWC wave energy converter [9]. In a recent investigation, Rodríguez et al. (2023) examined the hydrodynamic behavior of L-shaped OWC devices under random wave conditions. Their findings indicated that pressure levels at specific positions, including outside, inside, and near the front wall tip, escalate with higher wave heights. Notably, the pressure within the chamber demonstrated an increase during the occurrence of short-period waves [10].

The researchers concluded that using an L-shaped front wall with a reduced inlet channel length relative to the chamber length can enhance the average power output in long waves. Several research studies have tested the performance of conventional chamber designs or designs with simplified geometries. Our research, however, focused on testing the performance of a 3D chamber geometry design that was completed and commissioned in 2023, using different characteristic wave variations compared to its existing test trials. In 2019, Wave Swell Energy (WSE) Australia successfully developed an L-shaped OWC system. Under specific wave conditions, the UniWave200, a product of WSE's technology (Figure 1(A) and 1(B)), has the capability to generate sufficient energy to power 200 homes. The WSE technology achieves an impressive energy conversion efficiency of 48% by harnessing wave energy, which is subsequently converted into electricity on King Island, where the system is installed [11].

This paper aims to investigate the influence of wave height and wave period on the airflow and pressure differences in the L-shaped OWC chamber. The input waves in the conducted study varied with the characteristics of short waves. The model design of the L-shaped OWC chamber developed by WSE was obtained from a report written by Brown & Justin (2019) (Figure 2(A) and 2(B)) [12]. By establishing this relationship, the study primarily focuses on assessing the efficiency of the L-shaped Chamber OWC design developed by Wave Swell Energy in harnessing incoming wave energy potential.

2. Materials and methods

2.1. Model test

The numerical simulation software or Computational Fluid Dynamics (CFD) tool used in this research is Flow 3D version 11. The experimental model design used in the conducted research is an L-shaped OWC chamber developed by WSE Australia. The geometry of the experimental model is validated through experimental testing, with a scale ratio of 1:8 (Figure 2(A) and 2(B)).

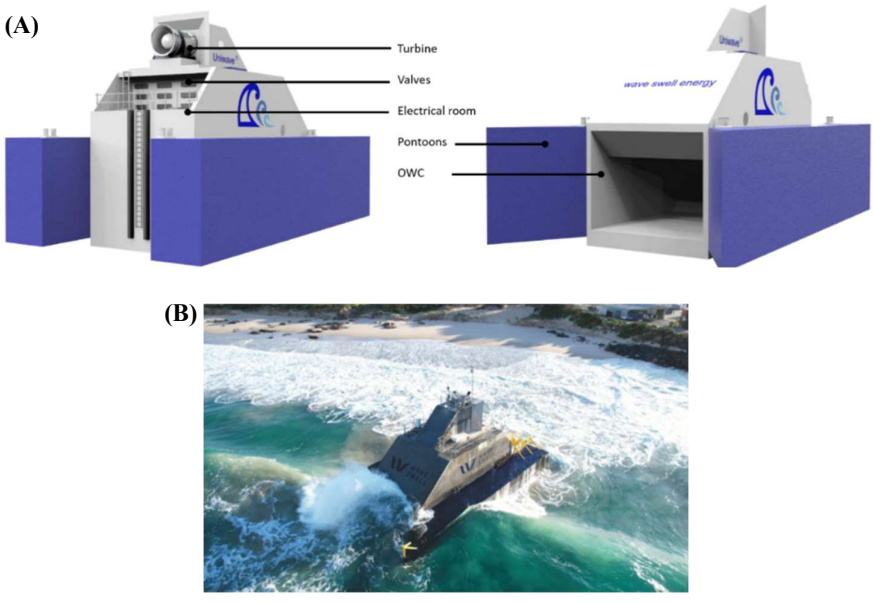

Figure 1 Development of the L-shaped OWC [12]: (A) The key features of the UniWave 200; (B) The installation and testing of the L-shaped OWC at Grassy Harbor Wave Swell Energy in 2023.

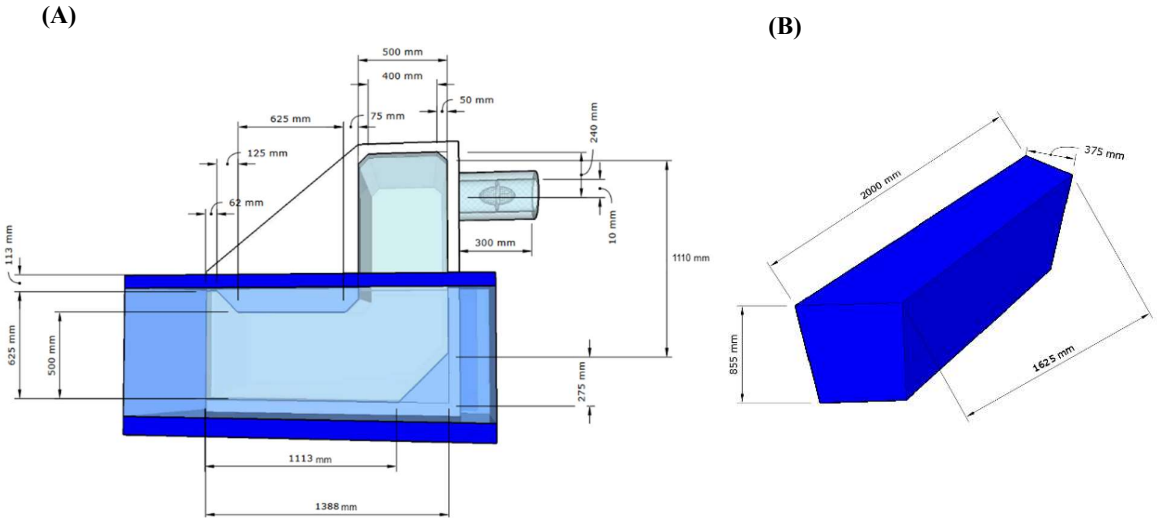

Figure 2 Model test of the OWC L-Shaped: (A) L-shaped Chamber geometry design; (B) pontoon geometry design.

2.2. Governing equations

The governing equations consist of the Navier-Stokes and continuity equations governing the flow of an incompressible Newtonian fluid. In their vector form, the equations are expressed as follows:

$$\rho\left(\frac{\partial v}{\partial t}+v.\nabla v\right)=\nabla P+\mu\nabla^2 v+\rho g \quad (1)$$

$$\nabla.v=0 \quad (2)$$

where p is the density of the fluid, P is the pressure, v is the velocity, μ is the dynamic viscosity, *g* is the acceleration of gravity, *t* represents the time, and ∇^2 is the vector Laplacian.

In this OWC numerical simulation, two fluids are used: water and air. The simulation represents an open-channel flow, necessitating the activation of gravity along the z-axis with a value of -9.81 m/s². The Volume of Fluid (VOF) method involving two distinct fluids is utilized for the analysis of the OWC [13–15]. The VOF method is employed for tracking the elevation of the free surface and is utilized to forecast and delineate the interface between air and water [16]. The equation for the volume fraction is:

$$\frac{\partial f_m}{\partial t}+\nabla.(f_m.U)=0 \quad (3)$$

where U is the velocity field, m = 0,1 for the phase of water and air; is the volume fraction bounded by $0 \le f_m \le 1$; $f_m = 1$ denotes that the grid is fully occupied by m^{th} fluid, $f_m = 0$ represents no m^{th} fluid exists in the grid, and $0 < f_m < 1$ means that there is an interface between water and air fluid.

Properties used in momentum equations, such as density and viscosity in interface grids, can be determined from the volume fraction of two phases [17]. The density and viscosity of the grids on the free surface can be expressed as:

$$\rho = f_0\,\rho_0 + f_1\,\rho_1 \quad (4)$$

$$v = f_0\,v_0 + f_1\,v_1 \quad (5)$$

Where *p* is the fluid density, is the kinematic viscosity, and is the volume fraction. In addition, the subscript 0 is for water, and the subscript 1 is for air.

The Renormalization Group (RNG) turbulence model is specifically utilized to derive average values related to turbulence, such as turbulent energy and dissipation rate, akin to the conventional k-ε turbulent model. Nevertheless, the constants employed in the RNG model are obtained from theoretical derivations, while those in the k-ε model are acquired from experimental data. FLOW-3D predominantly favors the RNG model over the k-ε model due to its capability to yield more precise outcomes in regions with low-intensity turbulence and shear fluid [18]. Furthermore, the k-ε renormalization group (RNG) turbulence model is employed to effectively represent and manage turbulent effects [19]. The governing equations for the k -ε RNG model are given as follows [20,21]:

$$\frac{\partial(\rho k)}{\partial t}+\frac{\partial(\rho k u_i)}{\partial x_i}=\frac{\partial}{\partial x_j}\left[\left(\mu+\frac{\mu_t}{\sigma_k}\right)\frac{\partial k}{\partial x_j}\right]+P_k-\rho\epsilon \tag{6}$$

$$\frac{\partial(\rho\epsilon)}{\partial t}+\frac{\partial(\rho\epsilon u_i)}{\partial x_i}=\frac{\partial}{\partial x_j}\left[\left(\mu+\frac{\mu_t}{\sigma_\epsilon}\right)\frac{\partial k}{\partial x_j}\right]+C_{1\epsilon}\frac{\epsilon}{k}P_k-C_{2\epsilon}^{*}\rho\frac{\epsilon^2}{k} \tag{7}$$

FLOW-3D employs another advanced advection algorithm based on a second-order, upwind-difference approach that preserves monotonicity [22]. This monotonicity-preserving technique is utilized in FLOW-3D to approximate the advection of momentum, density, energy, and fluid fraction. The discretization scheme of higher order is achieved through second-order polynomial approximations for the advected quantity in every coordinate direction [23]. For a variable Q being advected in the x-direction, the computed value of the flux through a cell-face, denoted as Q*, is calculated as follows:

$$Q^{*}=Q_i+\frac{1}{2}A(1-C)\delta x_i \tag{8}$$

where Q_i is the cell-centered value, $\frac{u\,.\,\delta t}{\delta x_i}$, C is the Courant number, and δx_i is the cell size. A is a second-order approximation to the first derivative of Q at the location $x_0\frac{1}{6}(1\text{-}2C)\,\delta x_i$ within the cell.

2.3. Computational fluid domain

The type of meshing used in this simulation is Cartesian meshing (Figure 3(A)). Cartesian meshing is a meshing technique that divides the simulation domain into cubic or quadrilateral mesh elements using Cartesian coordinates. The meshing process creates a grid-based on squares in the simulation domain [24]. The advantages of using Cartesian meshing in CFD Flow 3D are its capability to handle complex simulation domains effectively, produce high-quality grids, and accelerate computational time. This OWC simulation employs a multi-block meshing technique, specifically the nested-overlapped mesh (Figure 3(B)). The related mesh allows the creation of an attractive mesh area while limiting the number of computational cells. Nested mesh blocks are utilized to enhance resolution around the regions of interest. Moreover, finite element meshing for the embedded body can be used in the simulation to model fluid-structure interaction. This meshing technique offers flexibility to users in creating a simple and efficient mesh, thereby improving solver performance and reducing simulation turnaround time.

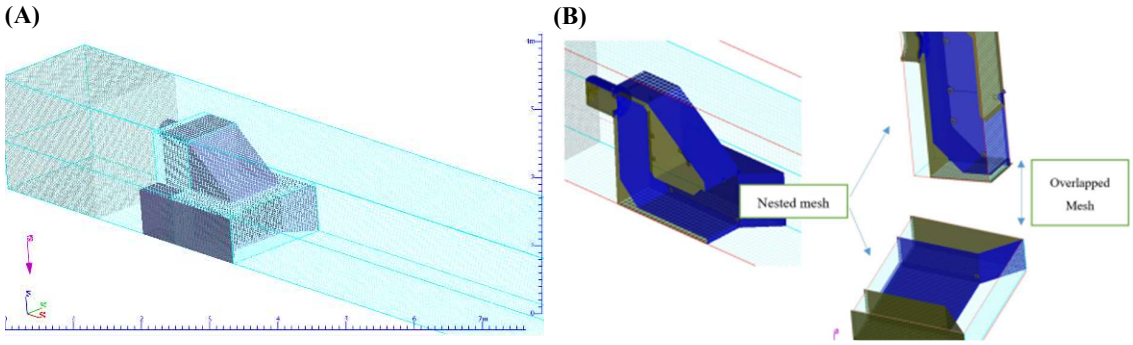

Figure 3 Meshing: (A) nested-overlapped block mesh; (B) block details.

The Fractional Area Volume Obstacle Representation (FAVOR) method is employed to assess the impact of meshing on the geometry [23]. Hexahedral mesh blocks are specified for the simulation, and there are 3 mesh blocks: block 1, block 2, and block 3. The mesh size for block 1 is 0.06, with an aspect ratio ranging from 1.09 to 1.001. On the other hand, the mesh size for blocks 2 and 3 is smaller, with a mesh size of 0.03 and an aspect ratio of 1.00. This choice of mesh size and aspect ratio aims to achieve efficiency and optimal results on the side of the OWC Chamber that interacts with the fluid.

The boundary conditions in this study are depicted in Figure 4. and consist of four main conditions. The length of the test channel in the simulation follows the hydralab III guidelines [25], with the wavelength being more than 3-5 times the length of the model's front. The width of the walls in the simulation is adjusted to the width of the test model. For the boundary conditions, the upstream inlet is determined using the wave height and period with the symbol (WV) and varied according to the test scenarios or matrix (Table 1). A periodic, linear surface wave can be produced at a mesh boundary. The model relies on a linear wave theory formulated by George Biddell Airy [23]. The linear wave is presumed to emerge from a flat bottom reservoir into the computational domain. A linear wave is characterized by the wavelength λ, wave frequency ω, wave number k=2π/λ, and wave amplitude A. The free surface elevation in the wave can be described by its coordinate in the vertical direction z = η(x,t), where

$$\eta = A \cos (kx - \omega t + \varphi) \tag{9}$$

Where φ is the phase shift angle, the amplitude of the wave (A) is smaller than the depth of water (h) and wavelength (λ). The wave speed c = ω/k is expressed as:

$$c^2 = \frac{g\lambda}{2\pi} \tanh \frac{2\pi h}{\lambda} \tag{10}$$

The downstream is defined as an outflow boundary with wave absorbing or wave dampening set to a width of 2 meters. The bottom boundary condition is defined as a wall with the symbol (W). The no-slip and no-penetration wall boundary conditions are applied as done by Trivedi et al. (2023) [26]. The sides of the channel are defined as symmetry (S). Consequently, it is anticipated that the intended physical geometry, flow pattern, and thermal solution will exhibit symmetrical characteristics. The upper boundary condition represents a free surface with a stagnation pressure (P) of 1 atm (101325 Pa) and 0.5 fluid fraction to account for air-water interactions.

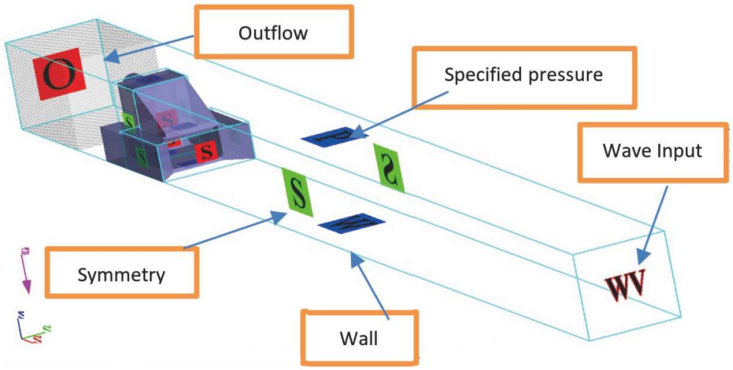

Figure 4 Boundary Conditions**.**

The data acquisition for this simulation involves three types of probes: free surface/wave gauges, pressure gauges, and airflow meters (Figure 5). Wave gauges are placed at the inlet of the wave generator, in front of the model structure, and in the middle of the OWC chamber. They are used to measure and monitor the free surface and wave characteristics. Pressure gauges are placed on the OWC chamber and the turbine orifice to obtain differential pressure data. These gauges help analyze the pressure distribution and changes in the system. The airflow gauge is positioned at the center of the turbine orifice to measure and assess the airflow behavior, as well as the incoming and outgoing airflow velocity in the OWC system. The numerical testing comprises variations in input wave height and wave period. There are a total of four variations in wave height and four variations in wave period, as detailed in Table 1. These simulated wave variations are designed to mimic the characteristics of waves in eastern Indonesia, specifically representing regular waves. The design of an L-shaped OWC chamber with a turbine diameter scenario of 0.2 meters and a water depth at Mean Sea Level (MSL) of 0.75 meters. The testing scale is set at 1:8, matching the experimental validation scale that has been conducted.

Table 1 Numerical test conditions.

Parameter	Variables
H_{in} (m)	0.0626; 0.125; 0.1875; 0.25
T_{in} (s)	1.41; 1.77; 2.12; 2.47

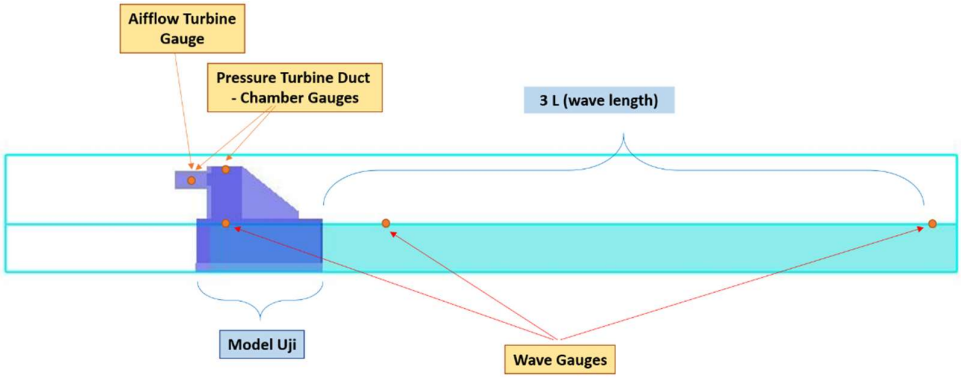

Figure 5 Numerical set-ups.

2.4 Dimensional analysis

The wave spectrum is typically summarized using a small number of parameters, most of which are calculated using spectral moments defined as follows:

$$P_{\text{wave front}} = \frac{P_{\text{water}} .g.h^2.\lambda}{16\ T} + \frac{1 + 4\ \pi\ d / \lambda}{\sinh (4\ \pi\ d/\lambda)} \tag{11}$$

The power of wave energy is defined as the wave power per meter of incoming ocean waves directed toward the wave energy converter (WEC) device. Hence, in a general sense, the power of incoming ocean waves can be formulated as follows [27]:

$$P = \frac{\rho g^2}{64\pi} H_{m0}^2 T_e \approx \left(0.5 \frac{kW}{m^2 s}\right) H_{m0}^2 T_e \tag{12}$$

The input power within the duct of an OWC-type wave energy turbine is influenced by both the airflow rate and the incoming airflow velocity into the turbine. This input power is formulated as follows [28] :

$$P_{in} = \left(dP + \rho \frac{v^2}{2}\right) A.v \tag{13}$$

In equation (13), where P_{in} represents the input power on the OWC turbine (Watts); dP is the differential pressure in the turbine duct (Pascal); ρ_{air} is the air density (Kg/m³); v is the airflow velocity (m/s); A, in this context, signifies the cross-sectional area of the turbine duct, measured in square meters (m²), the obtained energy can rotate the turbine in a wave energy power plant similarly to how airflow spins a wind turbine or wind power plant.

$$P_{\text{in airflow}} = \frac{1}{2}\ \rho.A.v^3 \tag{14}$$

In the OWC turbine, in addition to the energy caused by the airflow entering from the chamber towards the turbine, there is also a differential pressure (dP*)* between the pressure inside the chamber and the pressure in the turbine area. This pressure difference contributes to the power generated by the differential pressure.

$$P_{\text{in dP}} = dP.A.v \tag{15}$$

The source of energy in the OWC Wave Power Plant is the turbine, as evident from equations 14 and 15. The turbine generates power due to the energy acquired from both airflow and differential pressure. The presence of airflow and differential pressure is a result of the fluctuating water movement entering the chamber – pneumatic energy geometry, which subsequently rotates the turbine and produces electrical power. The geometry of the chamber is the primary component of the OWC Wave Power Plant that captures the water mass or energy from the incoming ocean waves. The efficiency coefficient of the chamber design is expressed as:

$$\eta = {}^{P_c}/_{P_{av}} \tag{16}$$

Where η *i*s power coefficient, P_c is power capture (13), P_{av} is available to power (12). The shape of this chamber's geometry influences the oscillation of the water inside the chamber, leading to the generation of airflow and differential pressure, which is then converted into electrical energy.

3. Result and discussion

3.1. CFD model validation

The key necessity in the verification and validation process is the grid-independent numerical solutions, commonly achieved through extrapolation methods [29]. The Grid Resolution approach determines mesh size using prior insights into the problem's physics. Mesh size is gradually increased until no substantial improvement in performance is observed with further mesh refinement [30]. In this study, a mesh independence study was conducted, as illustrated in Figure 6, with the graph indicating the mesh size that can be utilized in this simulation, which is smaller than 0.045. For this simulation work, a mesh size of 0.04 was used, which fulfills the criteria of the mesh independence study.

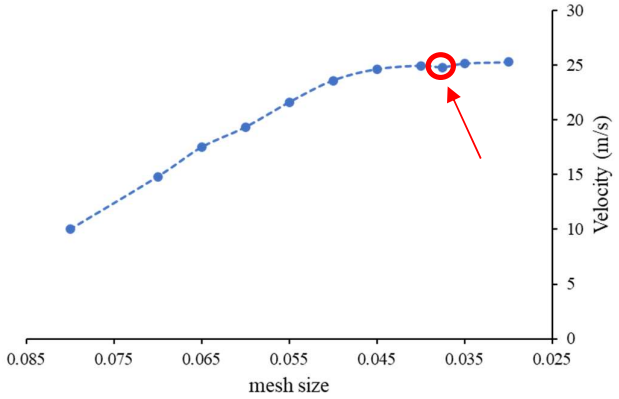

Figure 6 Mesh Independence Study.

Validation of numerical and experimental data involves the use of wave measurement data in the chamber area and pressure data inside the L-shaped chamber (Figure 7(A) and 7(B)) [31]. In Figure 8A, the validation results are shown between wave heights in the chamber area, with a Root Mean Square Error (RMSE) value of 0.07. The difference between numerical simulation and experimental data arises because, in the numerical simulation, the input waves match the testing scenario, while in the experiment, a 10-second ramp-up is required in the mechanical setup before forming the input waves as per the testing scenario (Figure 8A circled in green).

(A) **(B)**

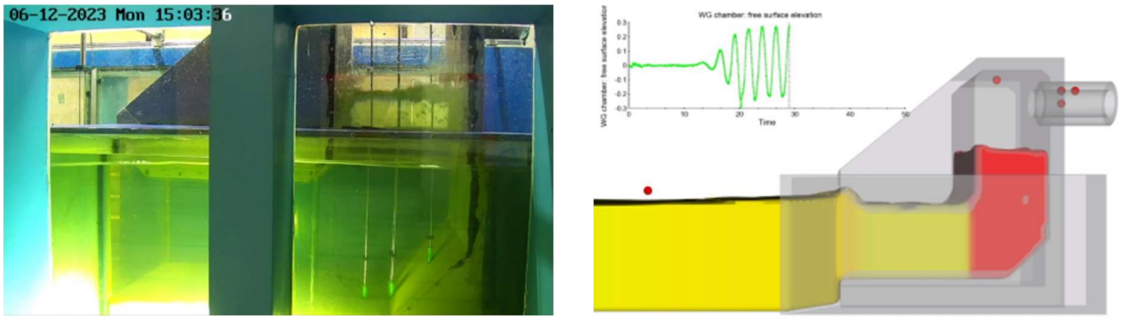

Figure 7 Comparison of water surface oscillations in experiments and numerical simulations; (A) experimenta and (B) numerical simulation.

In addition to wave height isolation inside the chamber, to achieve optimal validation results, a comparison was made between the numerical results of pressure differences and the experiments that were conducted. Figure 8B shows the coefficient of determination defined as R-squared (R^2) for the comparison of numerical and experimental results. The R^2 value for the pressure difference comparison is 0.9993. This result indicates the reliability and consistency of the numerical simulation concerning experimental results.

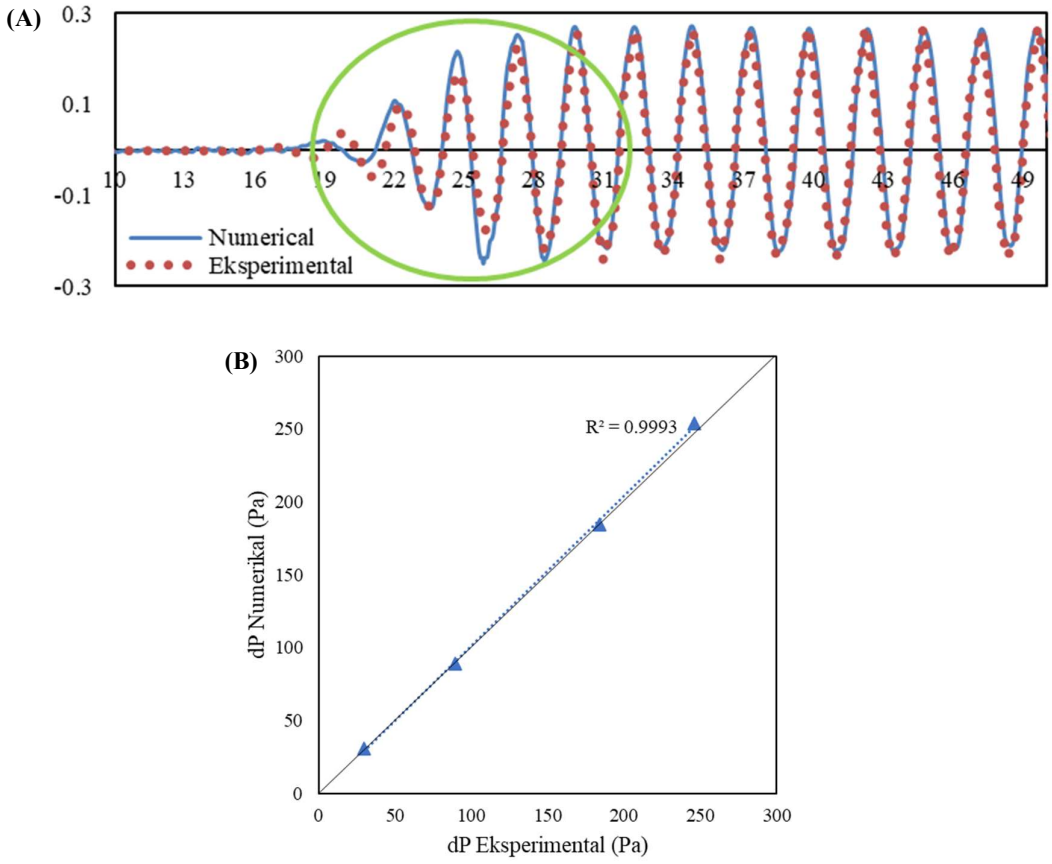

Figure 8 (A) Comparison of time-series wave height isolation in numerical simulation and experimental chamber, (B) The results of the comparison of numerical and experimental air differential pressure.

3.2 The influence of wave height and period on the airflow velocity

In Figure 9, it can be observed that the input wave height (H_{in}) and input wave period (T_{in}) have an impact on the airflow velocity (V_{air}) in the ducted turbine. The airflow velocity increases proportionally with the increase in Hin and Tin. The lowest airflow velocity is recorded at H_{in} = 0.0625 m and T_{in} = 1.41 s, at 1.84 m/s, while the highest airflow velocity is recorded at H_{in} = 0.25 m and T_{in} = 2.47 s, at 19.83 m/s. The graph (Figure 9) illustrates a trend where airflow velocity (V_{air}) exceeding Hin = 0.25 m does not significantly affect the increase in airflow velocity in this L-shaped OWC turbine duct (as indicated by the differences with the green and purple lines).

Figure 10 illustrates a direct correlation between wave oscillation inside the chamber ($H_{chamber}$) and airflow velocity (V_{air}), which increases as Hin and Tin are raised. When H_{in} and T_{in} increase, a larger volume of water enters the L-shaped chamber through the openings, resulting in higher oscillation inside the chamber. Consequently, this causes the airflow to increase both in and out of the turbine. The largest water oscillation in the chamber ($H_{chamber}$) occurs at the highest airflow velocity (V_{air}), when H_{in} = 0.25 m and T_{in} = 2.47 s, with a water oscillation of $H_{chamber}$ = 0.74 m. Conversely, when the $H_{chamber}$ is small, V_{air} in the turbine duct is also small. This indicates that $H_{chamber}$ is directly proportional to V_{air}.

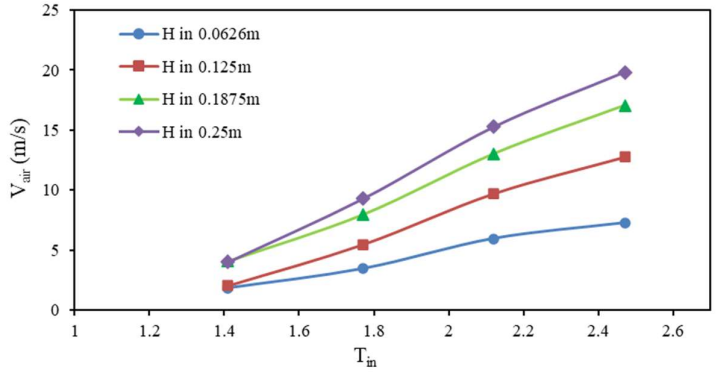

Figure 9 The influence of H_{in} and T_{in} on the airflow velocity.

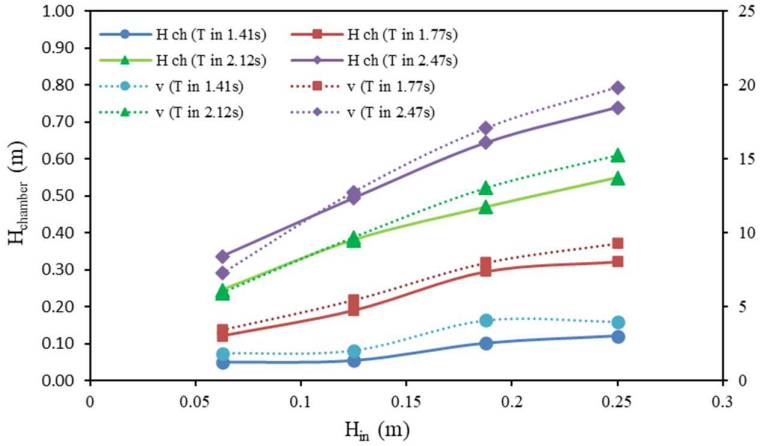

Figure 10 The relationship between H_{in} and T_{in} on water oscillation inside the chamber and airflow velocity.

3.3 The influence of wave height and wave period on differential pressure

Figure 11 illustrates that the influence of wave height (H_{in}) and wave period (T_{in}) significantly affects the differential pressure (dP) between the OWC chamber and the turbine duct. Similar to the effect on airflow velocity, the differential pressure increases in parallel with the increase in Hin and Tin. The smallest differential pressure is recorded at H_{in} = 0.0625 m and T_{in} = 1.44 s, which is 5.96 Pascal, while the highest is recorded at H_{in} = 0.25 m and T_{in} = 2.47 s, which is 253.81 Pascal. Unlike Figure 9, Figure 11 shows a trend where an increase in the pressure difference (dP) exceeding H_{in} = 0.25 m (purple line) potentially significantly increases the differential pressure in the chamber and turbine duct area. The L-shaped OWC system design continues to perform well and shows improved performance with longer wave periods, especially beyond T_{in} = 2.47 seconds.

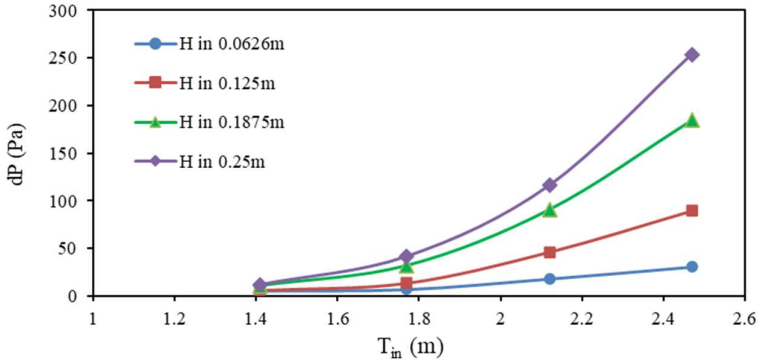

Figure 11 The influence of H_{in} and T_{in} on the differential pressure.

Figure 12 shows a direct correlation between wave oscillation inside the chamber ($H_{chamber}$) and the differential pressure (dP) between the chamber and the turbine duct, both of which increase with rising Hin and Tin. Higher wave height and wave period lead to a larger volume of water entering and exiting the chamber through the openings, resulting in an increase in dP within the chamber area. Additionally, higher water oscillation inside the chamber creates a greater pressure difference between the inside of the chamber and the external atmosphere. Similar to Figure 10, the highest water oscillation in the chamber, $H_{chamber}$ = 0.74 m, results in a high differential pressure compared to others, namely dP = 253.81 Pascal. The lowest oscillation inside the chamber, among others, at $H_{chamber}$ = 0.05 m, produces the lowest differential pressure. This indicates that $H_{chamber}$ is directly proportional to dP.

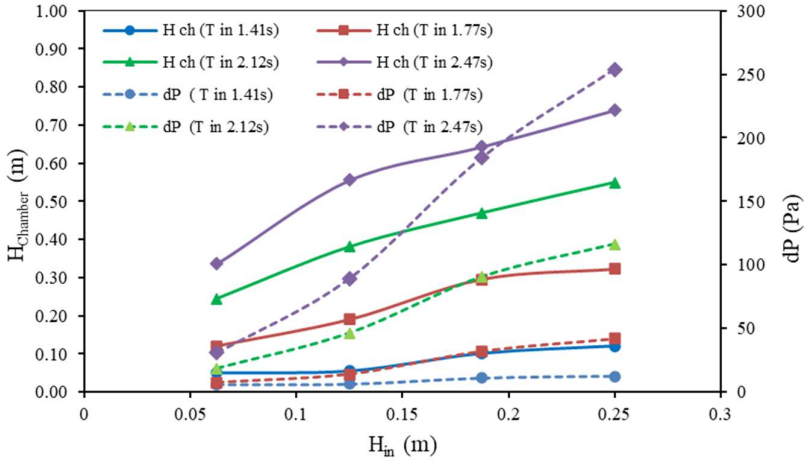

Figure 12 The relationship between H_{in} and T_{in} on water oscillation inside the chamber ($H_{chamber}$) and differential pressure (dP).

3.4 The influence of airflow velocity and differential pressure on power (P_{in})

The increase in power (watts) is directly proportional to the increase in V_{air} (m/s) and dP (Pa), as seen in Figure 15. The power generated is balanced and influenced by V_{air} and dP (Equations 2.14 and 2.15). The optimal power achieved in this study reached 80 watts with H_{in} of 0.25 m and T_{in} of 2.47 s. The influence of T_{in} (in Figure 15) shows a comparison between H_{in} 0.25 m with T_{in} 1.41 s (blue line) and T_{in} 2.47 s (purple line). The L-shaped OWC chamber design is more optimal, with wave generation having a longer period exceeding 2.12 seconds.

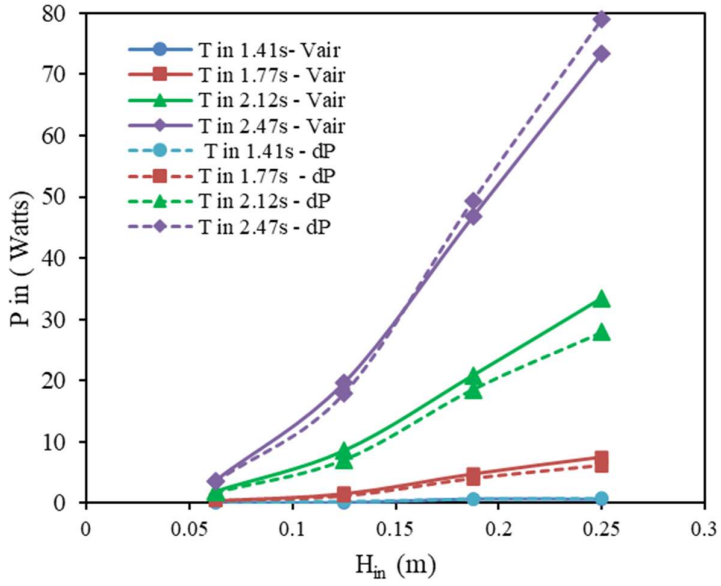

Figure 15 The relationship between airflow velocity and differential pressure on power (P_{in}).

3.5 The power efficiency of the OWC chamber L device with input variations H_{in} and T_{in}

The tested L-shaped chamber design exhibits intriguing characteristics worthy of attention. The efficiency of this chamber design is highly sensitive to the wave period or wavelength input. As shown in Figure 16, this design is optimized at a period of T_{in} 2.47 s, with an average efficiency across all wave height scenarios of 84.2%. Table 2 demonstrates the power efficiency generated from each wave generation scenario.

Table 2 Power efficiency (Equation 16) captured by the L-shaped chamber device divided by the available power based on theory.

$H_{in\,(m)}$ \ $T_{in\,(s)}$	1.41	1.77	2.12	2.47
0.0626	3.7	9.9	39.5	65.2
0.125	1.1	8.7	42.0	86.2
0.1875	2.4	12.5	46.9	98.2
0.25	1.4	10.9	41.1	87.6

Optimal efficiency is achieved at H_{in} 0.1875 m and T_{in} 2.47s, with an efficiency reaching 98.2%. Interestingly, as H_{in} is increased to 0.25 m, the efficiency tends to decrease, and this tendency continues to increase with the rise in T_{in}.

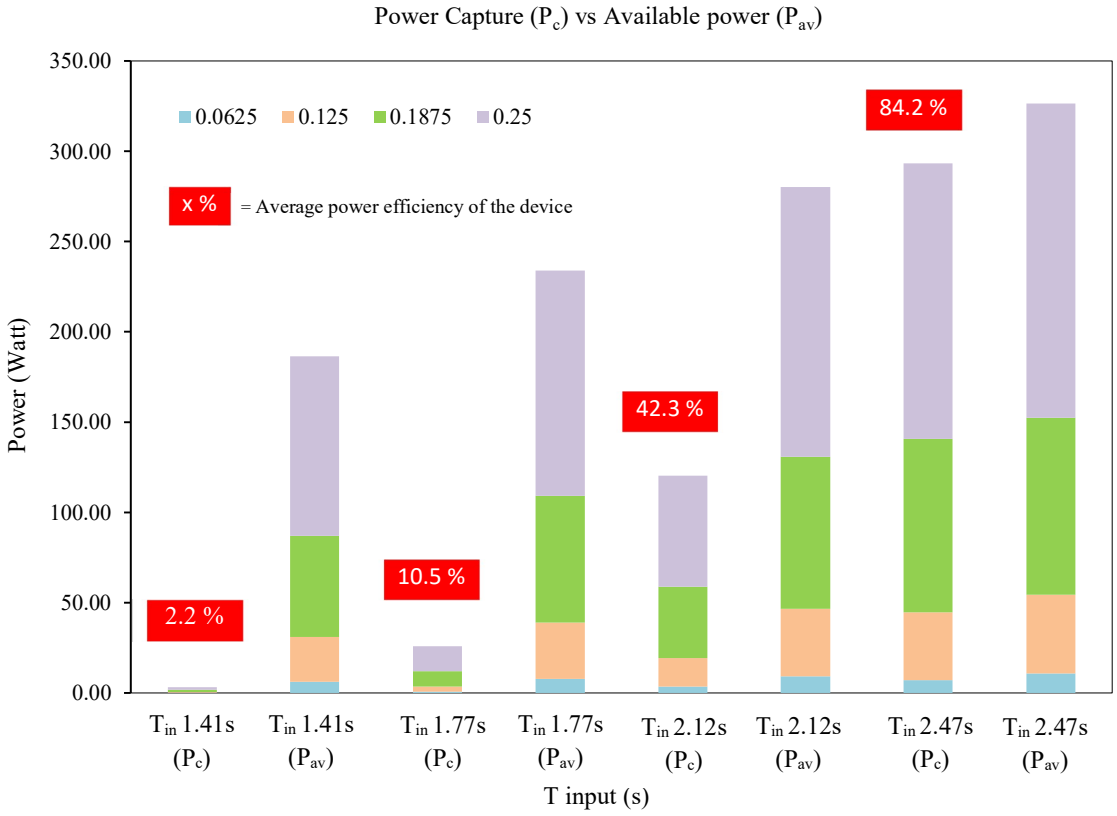

Figure 16 Comparison of power capture (P_c) with available power (P_{av}).

4. Conclusion

The research findings conclude that changes in wave height and wave period inputs significantly influence wave confinement within the chamber, thereby affecting airflow velocity and differential pressure in both the chamber and the turbine duct. Increasing wave height and wave period inputs increases water oscillation inside the chamber, leading to higher airflow velocity and differential pressure. The increase in airflow velocity and differential air pressure affects the increase in power in the L-OWC system. Wave height inputs exceeding 0.25 m do not result in a significant increase in airflow velocity and differential pressure inside the turbine and L-OWC

channel. However, the L-OWC system design functions well and exhibits increased power output with longer wave periods, especially exceeding wave period inputs of 2.12 sec. The power generated by the airflow velocity and differential pressure is nearly consistent at 80 watts. The chamber design is optimized at a period of T_{in} 2.47 s, with an average efficiency across all wave height scenarios of 84.2%. Optimal efficiency is achieved at H_{in} 0.1875 m and T_{in} 2.47s, with an efficiency reaching 98.2%.

5. Acknowledgments

Acknowledgments to the DPL-DIRI-BRIN team for their invaluable support in validating the numerical simulation data through experimental tests carried out in the coastal engineering laboratory. The experimental endeavors received backing from the House Program of New and Renewable Energy, Research Organization for Energy and Manufacture, BRIN, Indonesia, under grant number 13/III.3/HK/2022.

6. References

[1] Falnes J. A review of wave-energy extraction. Mar Struct. 2007;20(4):185–201.
[2] Czech B, Bauer P. Wave energy converter concepts : Design challenges and classification. IEEE Ind Electron Mag. 2012;6(2):4–16.
[3] Elhanafi A. Prediction of regular wave loads on a fixed offshore oscillating water column-wave energy converter using CFD. J Ocean Eng Sci. 2016;1(4):268–283.
[4] Juan NP, Valdecantos VN, Esteban MD, Gutiérrez JSL. Review of the Influence of Oceanographic and Geometric Parameters on Oscillating Water Columns. J Mar Sci Eng. 2022;10(2):226.
[5] López I, Carballo R, Fouz DM, Iglesias G. Design selection and geometry in owc wave energy converters for performance. Energies. 2021;14(6):1–18.
[6] Chen J, Wen H, Wang Y, Wang G. A correlation study of optimal chamber width with the relative front wall draught of onshore OWC device. Energy. 2021;225:120307.
[7] Ning DZ, Wang RQ, Zou QP, Teng B. An experimental investigation of hydrodynamics of a fixed OWC Wave Energy Converter. Appl Energy. 2016;168:636–648.
[8] Trivedi K, Ray AR, Krishnan PA, Koley S, Sahoo T. Hydrodynamics of LIMPET type OWC device under Stokes second-order waves. Ocean Eng. 2023;286(115605):115605.
[9] Samak MM, Elgamal H, Nagib Elmekawy AM. The contribution of L-shaped front wall in the improvement of the oscillating water column wave energy converter performance. Energy. 2021;226:120421.
[10] Medina Rodríguez AA, Posada Vanegas G, Vega Serratos BE, Oderiz Martinez I, Mendoza E, Blanco Ilzarbe JM, et al. The hydrodynamic performance of a shore-based oscillating water column device under random wave conditions. Ocean Eng. 2023;269:113573.
[11] Hayward J. Wave energy cost projections: A report for Wave Swell Energy Limited [Internet]. Australia: CSIRO Energy, Australia's National Science Agency; 2021. [cited 2024 Mar 9]. Available from: https://www.csiro.au.
[12] Brown D. UniWave200 King Island [Internet]. Tasmania, Australia: Wave Swell Energy Ltd; 2019. [cited 2024 Feb 10]. Available from: https://www.projecte.com.au.
[13] Vyzikas T, Deshoulières S, Giroux O, Barton M, Greaves D. Numerical study of fixed oscillating water column with RANS-type two-phase CFD model. Renew Energy. 2017;102:294–305.
[14] Gurnari L, G.F.Filianoti P, M.Camporeale S. Fluid dynamics inside a U-shaped oscillating water column (OWC): 1D vs. 2D CFD model. Renew Energy. 2022;193:687–705.
[15] Liu Z, Hyun BS, Hong K. Numerical study of air chamber for oscillating water column wave energy convertor. China Ocean Eng. 2011;25(1):169–178.
[16] C.W. Hirt and B. D. Nichols. Chaotic self-tuning PID controller based on fuzzy wavelet neural network model. J Comput Phys. 19981;39:201–225.
[17] Wu HL, Hsiao SC, Lin TC. Evolution of a two-layer fluid for solitary waves propagating over a submarine trench. Ocean Eng. 2015;110:36–50.
[18] Kuo YS, Chung CY, Hsiao SC, Wang YK. Hydrodynamic characteristics of oscillating water column caisson breakwaters. Renew Energy. 2017;103:439–447.
[19] Liu Z, Xu C, Kim K, Choi J, Hyun B soo. An integrated numerical model for the chamber-turbine system of an oscillating water column wave energy converter. Renew Sustain Energy Rev. 2021;149:111350.
[20] Yakhot V, Orszag SA. Renormalization group analysis of turbulence. I. Basic theory. J Sci Comput. 1986;1(1): 3–51.
[21] Yakhot V, Smith LM. The renormalization group, the ε-expansion and derivation of turbulence models. J Sci Comput. 1992;7(1):35–61.
[22] van Leer B. Towards the ultimate conservative difference scheme. V. A second-order sequel to Godunov's method. J Comput Phys. 1979;32(1):101–136.

[23] Flow Science, Inc. FLOW-3D User Manual: Version 9.3. [Internet]. Santa Fe, NM: Flow Science, Inc.; 2008. [cited 2023 oct 9] Available from: https://www.flow3d.com
[24] Qu M, Yu D, Xu Z, Gao Z. The effect of the elliptical front wall on energy conversion performance of the offshore OWC chamber: A numerical study. Energy. 2022;255:124428.
[25] Wolters G, Van Gent M, Allsop W, Hamm L, Mühlestein D. HYDRALAB III: Guidelines for physical model testing of rubble mound breakwaters. In: Coasts, marine structures and breakwaters: Adapting to change. London: Thomas Telford Ltd; 2010. p. 559-670.
[26] Trivedi K, Ray AR, Krishnan PA, Koley S, Sahoo T. Hydrodynamics of an OWC device in irregular incident waves using RANS model. Fluids. 2023;8(1):1–31.
[27] Mishra SK, Appasani B, Jha AV, Garrido I, Garrido AJ. Centralized Airflow control to reduce output power variation in a complex OWC ocean energy network. Complexity. 2020;2020:1-16.
[28] Mishra S, Purwar S, Kishor N. Maximizing output power in oscillating water column wave power plants: An optimization based MPPT algorithm. Technologies. 2018;6(1):15.
[29] Seeni A, Rajendran P, Mamat H. A CFD mesh independent solution technique for low reynolds number propeller. CFD Lett. 2019;11(10):15–30.
[30] Almohammadi KM, Ingham DB, Ma L, Pourkashan M. Computational fluid dynamics (CFD) mesh independency techniques for a straight blade vertical axis wind turbine. Energy. 2013;58:483–493.
[31] Marta ASD, Deendarlianto, Kongko W, Aprijanto, Rohman AT, Wibowo A, et al. The Influence of Wave Characteristics, Tides, and Installation Conditions of L-Shaped OWC Wave Energy Converter on Energy Absorption Capability. Evergr Jt J Nov Carbon Resour Sci Green Asia Strateg. 2024;11(03):2607–2617.